Geophysical Research Letters

RESEARCH LETTER
10.1029/2022GL098708

The Oscillatory Motion of Jupiter's Polar Cyclones Results From Vorticity Dynamics

Nimrod Gavriel[1] **and Yohai Kaspi**[1]

[1]Department of Earth and Planetary Sciences, Weizmann Institute of Science, Rehovot, Israel

Key Points:

- The cyclones at Jupiter's south pole oscillate around their equilibrium positions with a ∼1 year period and a ∼400 km amplitude
- A poleward beta-drift force and mutual rejection forces between the cyclones are established as the drivers of the observed oscillations
- The suggested mechanism is supported both by observation-based calculations of accelerations and forces and by an ideal model simulation

Supporting Information:

Supporting Information may be found in the online version of this article.

Correspondence to:

N. Gavriel,
nimrod.gavriel@weizmann.ac.il

Citation:

Gavriel, N., & Kaspi, Y. (2022). The oscillatory motion of Jupiter's polar cyclones results from vorticity dynamics. *Geophysical Research Letters*, *49*, e2022GL098708. https://doi.org/10.1029/2022GL098708

Received 16 MAR 2022
Accepted 10 JUN 2022

Author Contributions:

Conceptualization: Nimrod Gavriel, Yohai Kaspi
Formal analysis: Nimrod Gavriel
Funding acquisition: Yohai Kaspi
Methodology: Nimrod Gavriel
Resources: Yohai Kaspi
Supervision: Yohai Kaspi
Validation: Nimrod Gavriel, Yohai Kaspi
Visualization: Nimrod Gavriel
Writing – original draft: Nimrod Gavriel
Writing – review & editing: Nimrod Gavriel, Yohai Kaspi

Abstract The polar cyclone at Jupiter's south pole and the five cyclones surrounding it oscillate in position and interact. These cyclones, observed since 2016 by NASA's Juno mission, present a unique opportunity to study vortex dynamics and interactions on long time scales. The cyclones' position data, acquired by Juno's JIRAM instrument, is analyzed, showing dominant oscillations with ∼12 month periods and amplitudes of ∼400 km. Here, the mechanism driving these oscillations is revealed by considering vorticity-gradient forces generated by mutual interactions between the cyclones and the latitudinal variation in planetary vorticity. Data-driven estimation of these forces exhibits a high correlation with the measured acceleration of the cyclones. To further test this mechanism, a model is constructed, simulating how cyclones subject to these forces exhibit similar oscillatory motion.

Plain Language Summary The poles of Jupiter, observed by NASA's Juno spacecraft since 2016, have a unique symmetric arrangement of storms, where a polar cyclone situated at each pole is surrounded by eight cyclones in the north pole and five cyclones at the south pole. These cyclones, traced for over 5 years, move with a circular periodic pattern with a 1 year cycle. Here, we explain these periodic patterns by considering the sum of the mutual rejection forces and the polar attraction force resulting from the conservation of momentum inside each cyclone. Using the cyclones' position data, a calculation of these forces agrees with their measured acceleration, supporting the suggested mechanism. In addition, a simplified model is constructed, which simulates how the south polar cyclones would move under these forces and predict the same type of circular motion.

1. Introduction

The poles of Jupiter were observed in detail for the first time by the Juno spacecraft in 2016 (Bolton et al., 2017). In contrast with the polar regions of Saturn, which are inhabited by a single polar cyclone (PC) (Baines et al., 2009; Sánchez-Lavega et al., 2006), Jupiter's PCs are surrounded by a ring of stable circumpolar cyclones (CPCs) (Adriani et al., 2018; Orton et al., 2017). There are eight CPCs at the north pole and five at the south (Figure 1), each with a diameter of roughly 5,000 km and velocities reaching 100 ms^{-1} (Adriani et al., 2020; Grassi et al., 2018). Such cyclones can be generated by moist convection (O'Neill et al., 2015, 2016), where 2D inverse energy cascade in the turbulent polar regions brings the kinetic energy from the convective scale up to the horizontal scale of the cyclones (Moriconi et al., 2020; Siegelman et al., 2022). These regions are bounded by prograde jets at around latitudes 65°N\S (Rogers et al., 2017, 2022), which may act as a separating barrier. In contrast with the Great Red Spot, which is centered around latitude 20°S and has a shallow depth (less than 500 km, Parisi et al. (2021)) relative to the deep surrounding jets (∼3,000 km, Kaspi et al. (2018)), the polar cyclones, subject to the Taylor-Proudman theorem (Vallis, 2017) with a vertical axis parallel to the planetary rotation axis and a smaller Rossby number, potentially extend deeper, suggesting a 2D dynamical regime.

The beta-drift is a force that results from a dipole of vorticity (usually termed "beta-gyres," Sutyrin and Flierl (1994)) that is induced by an interaction between the tangential velocity of a cyclone and a gradient of potential vorticity (PV) that is present in the background of the cyclone (Chan, 2005; Gavriel & Kaspi, 2021; Rossby, 1948). This force creates a poleward drift on cyclones and an equatorward drift on anticyclones when only the planetary vorticity gradient (β) is considered (Chan, 2005; Franklin et al., 1996; Merlis & Held, 2019). Beta-drift is a known contributor to the poleward motion of Earth's tropical cyclones (Zhao et al., 2009), and was shown in shallow-water (SW) models to result in cyclones merging into a PC in settings characterizing gas-giants such as Jupiter and Saturn (Brueshaber et al., 2019; Brueshaber & Sayanagi, 2021; O'Neill et al., 2016; Scott, 2011). Also, vortex crystals (Fine et al., 1995; Schecter et al., 1999) similar to Jupiter's

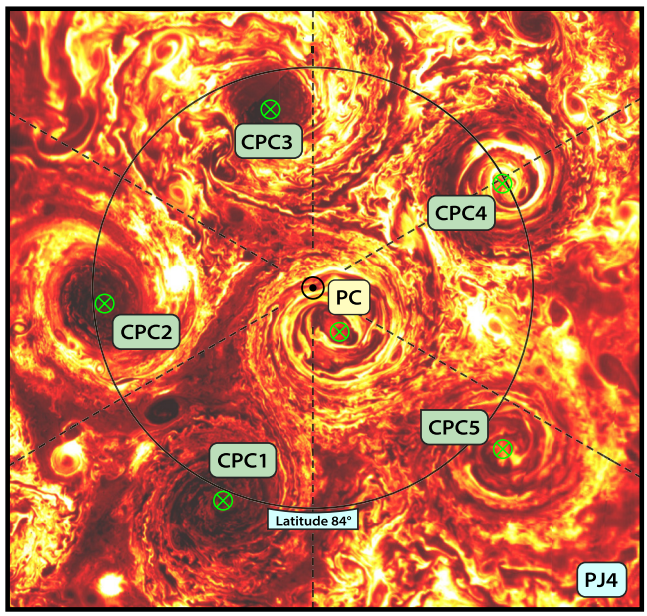

Figure 1. Infrared radiation photograph of Jupiter's south pole taken by the JIRAM instrument on Juno. Image credit: NASA/JPL-Caltech/SwRI/ASI/INAF/JIRAM. The black point represents the pole. The dashed lines represent intervals of 60° longitude (longitude 0° in System III is the line going "upward" from the pole). The green 'X's are the estimated location at the centers of the south polar cyclones during PJ4.

were shown to form around the pole from turbulent initial conditions under the influence of β in quasi-geostrophic (QG) model simulations (Siegelman, Young & Ingersoll, 2022). However, other theories for poleward drift of cyclones exist (Afanasyev & Huang, 2020; Afanasyev & Zhang, 2018). In addition to β, any PV gradient in the background of a cyclone (e.g., by a jet or a nearby cyclone) can similarly influence its motion (Chan & Law, 1995; Shin et al., 2006; Rivière et al., 2012). For example, the PV gradient due to the zonal mean wind shear and β was shown, using full 3D models, to drive the meridional motion of large vortices on Uranus (LeBeau et al., 2020) and Neptune (LeBeau & Dowling, 1998). It was recently found that latitude ∼84°, where the CPCs are observed at both poles of Jupiter, is the latitude where the beta-drift is balanced by an equivalent vorticity-gradient force, in which the source of the PV gradient field is the PC instead of the planetary β (Gavriel & Kaspi, 2021). Such a rejection force between cyclones is dependent on them having an anticyclonic ring around them (Li et al., 2020), often referred to as a 'vortex shielding', which is consistent with observations (Gavriel & Kaspi, 2021; Grassi et al., 2018; Ingersoll et al., 2021) and SW simulations of the polar cyclones (Li et al., 2020). This balance between the forces proved impossible on Saturn, as its PCs are too large, such that the annulus where they could reject CPCs is too far from the poles, where β dominates, thus inhibiting Saturnian CPCs (Gavriel & Kaspi, 2021).

The locations of the CPCs have been monitored since Juno's arrival at Jupiter (Adriani et al., 2020; Mura et al., 2021; Tabataba-Vakili et al., 2020). While the average locations of the cyclones match the calculations of Gavriel and Kaspi (2021) (hereafter GK21), the individual cyclones were found to oscillate around these stable positions, where perturbations seem to pass on between neighboring cyclones (Mura et al., 2021). In addition, an average westward drift of approximately 7.5° (3°) per year was measured on the cyclones at the south (north) pole (Adriani et al., 2020; Mura et al., 2021). Here, we extend the work laid out by GK21 and show that in addition to determining the equilibrium conditions of the CPCs, vorticity-gradient forces also control their observed oscillatory motion.

2. Results

2.1. Characterizing the Motion of the Cyclones in the Data

To analyze the motion of the PC and the CPCs, we use the data gathered by Juno's JIRAM instrument (Mura et al., 2021). As the measurements of the cyclones at the north pole were relatively infrequent, we make the analyses only for the south pole. Each orbit of Juno is termed a perijove (PJ), taking ∼53 days per orbit during the first 30 PJs analyzed in this study. An interpolation of the path that the cyclones went through between PJs is shown in Figure 2a, where the trajectories of the cyclones are divided by color to the 3 years and 9 months of observations between PJs 4 and 30. Considering for example, CPC2, it can be seen that the motion of the cyclone can be inferred as a circular ∼1 year oscillation with an amplitude of ∼3° longitude (or ∼0.3° latitude), orbiting an equilibrium point that migrates westward at ∼7° longitude per year.

We suggest here that this motion results from a dynamical system of six bodies (cyclones) with 15 spring-like connections (i.e., rejection forces as described in GK21) between them, in addition to the beta-drift polar attraction acting independently on each cyclone. This picture is illustrated for one cyclone in Figure 3, where the subject cyclone is rejected by the five other cyclones, where each rejection force decreases in magnitude with the distance between the cyclones, and is pushed toward the pole by the beta-drift force (F_β). The magnitude of F_β increases with distance from the pole (Gavriel & Kaspi, 2021). The net force (F_{tot}), resulting from the summation of the six forces, deflects the trajectory of the cyclone and results in a circular path concentric to the position of equilibrium. This scheme gets more complicated when taking into account that the five rejecting cyclones in Figure 3 move and oscillate as well, resulting in a more chaotic pattern, which includes various modes between the six cyclones. These interferences can be seen in the more complex paths of the six cyclones (Figure 2a). Note that

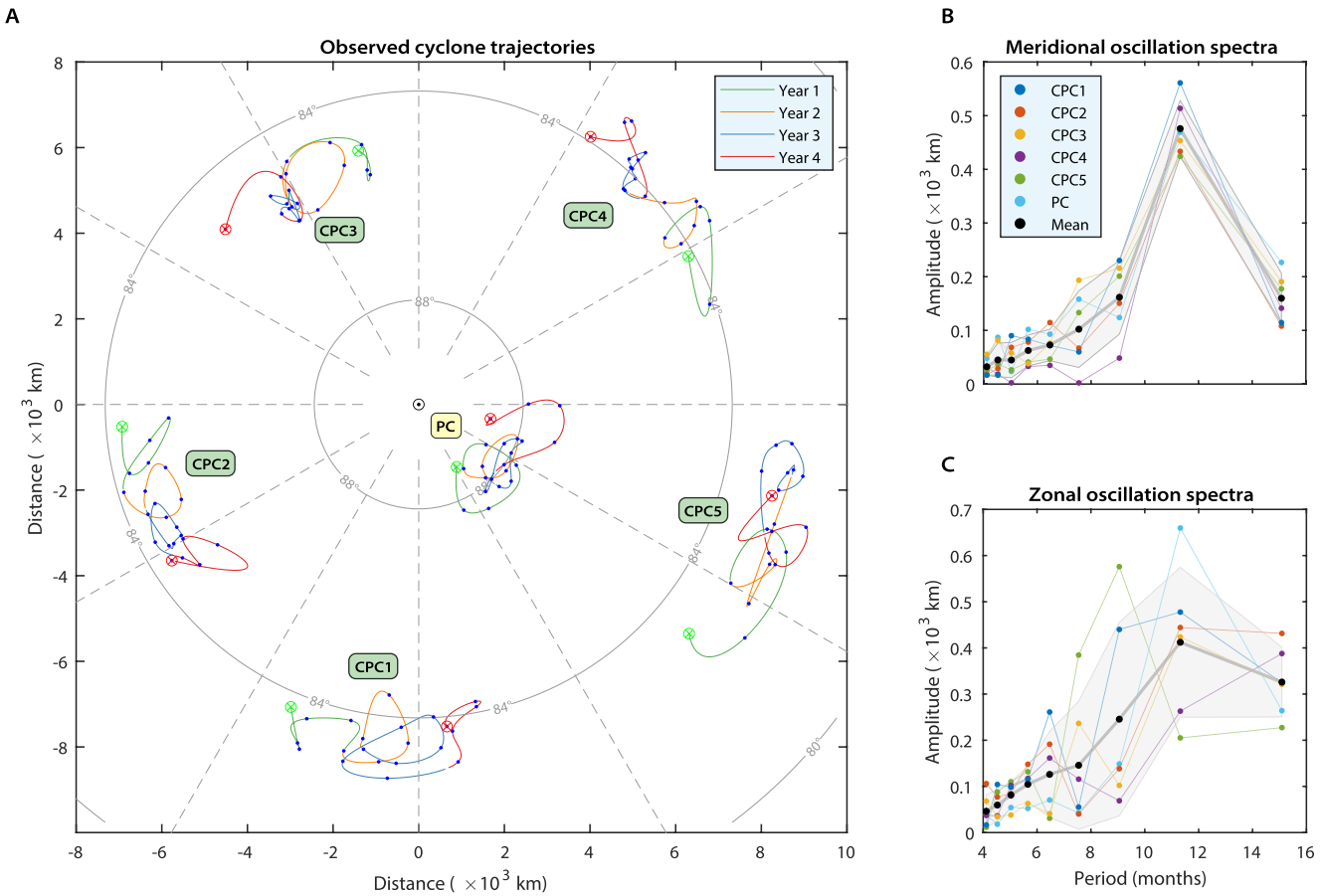

Figure 2. (a) The observed trajectories of the cyclones at the south poles. The green (red) 'X's represent the locations of the cyclones at PJ4 (30), which are the initial (final) locations in the tracked period. For context, see JIRAM's image from PJ4 (Figure 1). Dots represent observed coordinates (Mura et al., 2021). The lines are cubic "spline" interpolations between the dots, and are therefore speculative. The lines change their color in the passing of every year since PJ4 (second of February 2017). As the data contain less than 4 consecutive years, the red curves only represent 9 months. The black dot represents the pole, gray circles are latitude [°], and dashed gray lines represent intervals of 30° longitude (longitude 0° in System III is the line going "upward" from the pole). See Movie S1 for an animation of these trajectories. See Figure S2 in Supporting Information S1 for time series of the motion's longitude and latitude. (b and c) The frequency spectra of the observed meridional and zonal (interpolated) motion of the cyclones, respectively. Straight colored lines are linear interpolations between the calculated values (colored dots) and thus do not represent real spectra. Black dots represent the mean spectra between the six cyclones, and the gray shade represents a standard deviation (calculated between the six cyclones) around the mean. These spectra are presented in terms of oscillation energy in Figure S1 of Supporting Information S1. Notice that the time units presented in this study are Earth's years and months and therefore do not hold physical significance such as orbital periods.

the cumulative trajectory of the cyclones (Figure 2a) is not entirely concentric to the pole, but is displaced. This can happen, in the context of the suggested mechanism, if CPC2 and CPC3 "weigh" more than the other cyclones in terms of their rejection forces and their attraction to the pole, thus they get closer poleward while pushing the other cyclones father away.

To further dissect the observed motion, it is informative to look on the spectra of the observed motion in the meridional and zonal directions (Figures 2b and 2c). All of the cyclones have a dominant oscillation mode of a ~1 year period and ~400 km amplitude. In the zonal direction (Figure 2c), the spectrum is more dispersed, perhaps due to the absence of the regulating effect of the beta-drift in the zonal direction, leaving only the complex pattern of rejection forces that change in direction and magnitude with time, thereby creating more variety in the oscillation patterns. For details regarding the data analysis presented in Figure 2, see Section S1.1 in Supporting Information S1.

2.2. Estimation of the Vorticity-Gradient Forces - Comparison With the Measured Accelerations

To validate that the the observed motion (Figure 2) results from the hypothesized mechanism laid out in the previous section (Figure 3), it is possible to estimate the net force acting on each cyclone according to its latitude and

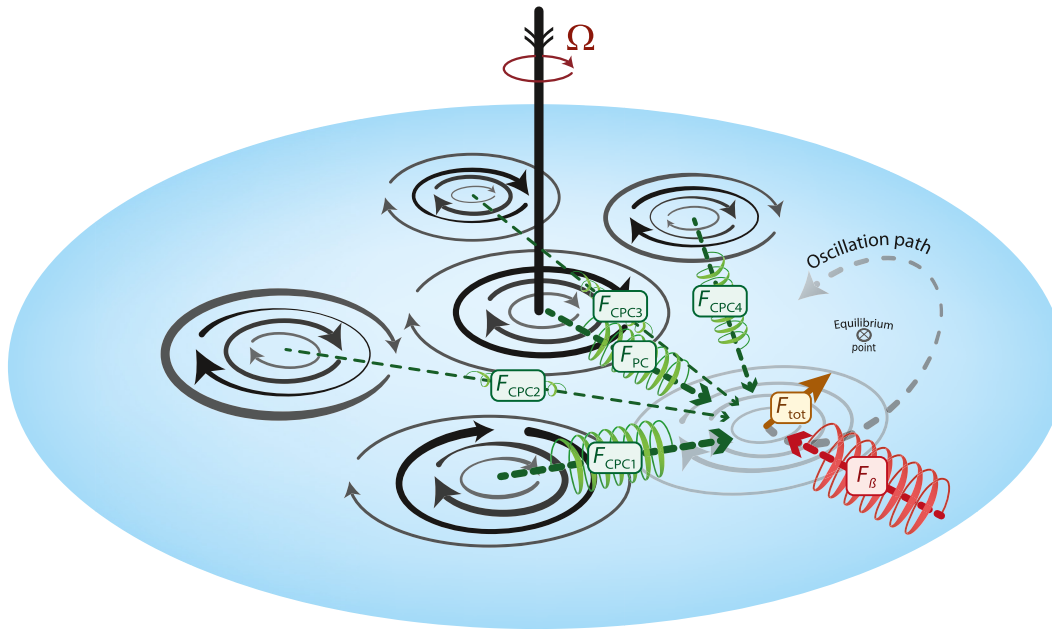

Figure 3. An illustration of the dynamical process driving the observed motion of the south polar cyclones. The thick black line in the center represents the planetary rotation axis and points to the pole. The green arrows and springs represent the rejection forces acting on a circumpolar cyclone (CPC) due to the vorticity-gradient forces by the individual cyclones. The direction of these forces might rotate by a small factor, as described in Section 2.2. The magnitude of the forces ($F_{\mathrm{CPC}i}$ by CPC number i, and F_{PC} by the polar cyclone (PC)), expressed qualitatively by the size of the arrows, decreases with the distance between the cyclones. Therefore, the far CPC2 and CPC3 exert minor rejection on the forced CPC. The red F_{β} represents the polar attraction due to the beta-drift. The blue shade represents the potential magnitude of F_{β} as a function of latitude, which vanishes (white shade) at the pole and gets larger (bluer shades) away from it. The brown arrow (F_{tot}) represents the total net force acting on the cyclone. F_{tot} points toward the equilibrium point, the location where the net force vanishes. The gray dashed arrow illustrates an oscillatory path around the equilibrium point. Due to the motion's inertia, the net force is perpendicular to the path. Note that the portrayed forces are more complex than a linear spring (e.g., they only "push" away from the source and never "pull" toward it), and thus the representation of them as springs is made only for illustrative purposes.

its distance from the other cyclones at each point in time. From Newton's second law, we expect that the acceleration ($\boldsymbol{a}_i$, where i is an index representing the respective cyclone on which the forces are calculated), estimated by differentiating the cyclone's observed position data in time, should match

$$\mathbf{a}_i = \underbrace{\sum_{j\neq i} \mathbf{F}_{ji} + \mathbf{F}_{\beta i}}_{F_{\mathrm{tot,i}}}, \tag{1}$$

where $\boldsymbol{F}_{\mathrm{ji}}$ is the rejection force vector (per unit mass) by cyclone j, and $\boldsymbol{F}_{\beta i}$ is the beta-drift force vector (per unit mass). The forces are "Rossby forces" (Rossby, 1948), calculated by a concentric integration of the Coriolis force around the cyclone, where the background vorticity alters respectively for each force term (See details in Section 1.2 in Supporting Information S1). These calculations require determining three global parameters, and three characteristic numbers for each of the six cyclones, which dictate their maximum velocity, their size and their morphology. These free parameters are chosen here to stay constant with respect to time, albeit in reality they may also have temporal variations.

To resolve these unknown parameters, an optimization procedure is used to provide the best overall match between the two sides of Equation 1. For the three cyclone characteristic numbers, up to 20% variability between cyclones was allowed (30% in the case of the morphology factor), relative to mean estimated values. Of the three global parameters determined by the optimization algorithm is K_{def}, which is the amount by which the forces are deflected clockwise. This deflection accounts for the fact that after the beta-gyres form, they can be advected by the tangential velocity of the cyclones (clockwise in the case of cyclones in the southern hemisphere) such

that the net force is deflected, to some extent, in the clockwise direction (Fiorino & Elsberry, 1989). In GK21, the analysis of the CPCs latitude of equilibrium assumed a balance between the PC's rejection force and the beta-effect; here, also taking into account the spatial distribution of the cyclones, we find that rejection of CPCs by CPCs also has a significant component in the meridional direction. The counter balance offered here against this effect, is that turbulence around the pole can partially homogenize the vorticity of the cyclones away from their centers, thereby diminishing their respective gradients and the resulting rejection forces. To take this into account, a factor K_{trb} is applied in the calculation of $\boldsymbol{F}_{\mathrm{ji}}$. The third global parameter is R_{int}, which determines what fraction of the cyclones' cores is being integrated to calculate the forces. The values determined for the unknown parameters and all other details of the calculations are elaborated in Section S1.2 in Supporting Information S1.

The resulting forces, calculated according to the observed instantaneous locations of the cyclones, exhibit a good match with the respective accelerations (Figure 4). This match is particularly pronounced when looking on CPC1 and CPC3; however, all cases achieve positive correlations (ρ in Figure 4) that are mostly higher than 0.5. Some mismatch between the curves may be a result of turbulence and impacts of cyclones which arrive at the polar region due to beta-drift and transfer momentum to the six cyclones. Such impacts would only directly affect the acceleration of the impacted cyclones, but would not have a signature in the calculation of the forces. To highlight this, two PJs (PJ18, Adriani et al. (2020), & PJ23, Mura et al. (2021)) when an intruder cyclone was observed in the polar ring are marked by purple lines (Figure 4), but the impact's effects may only take place at a specific time during the ∼3.5 months between the preceding PJ and the following PJ. In the meridional direction of the PC, the relatively low correlation might be expected, as the extremely low β (and therefore $\boldsymbol{F}_{\beta}$) near the pole leaves it more susceptible to noise. We note here that the acceleration time series presented in Figure 4, differentiated from the position data, which is spaced ∼53 days between data points, only give a measure of the long time-scale accelerations, while instantaneous accelerations can be somewhat different. This is reasonable for the comparison of the vorticity-gradient forces, which only act on long time-scales.

To reassure the reader that the implemented optimization cannot produce this match between acceleration and force out of thin air, we stress that all parameters are constant in time, which means that all the temporal trends in Figure 4, are direct consequences of the observational data. This implies that without having the underlying physics correct, it is not likely that any set of parameters would be able to produce correlations in the time series, let alone correlate well on the 12 independent cases (Figure 4). To support this statement, a test with 300 sets of random motion is generated and optimized with the same procedure as was done for Figure 4, showing very weak correlations between the random accelerations and the resulting forces (see Section. 1.2.5, and Figure S3 in Supporting Information S1). Also, the sensitivity of the results (Figure 4) to variations in the optimized parameters is analyzed in Figure S5 of Supporting Information S3. Overall, the match between the forces and the accelerations supports the claim that these vorticity-gradient forces indeed drive the observed motion of the cyclones.

One approach to support the results of Figure 4 is to analytically estimate the oscillations period from the vorticity-gradient forces. Here, we consider a simple harmonic oscillation of one CPC and two static neighbors in the zonal direction (Figure S6 in Supporting Information S1). Taking a derivative of the mean rejection force per unit mass (F) with a zonal perturbation (x_0) from the position of equilibrium gives the spring constant, from which the oscillation period (T_{N}) is derived (see full details in Section S2 in Supporting Information S1) as

$$T_{\mathrm{N}} = 2\pi \left(\frac{\partial F}{\partial x_0} \right)^{-\frac{1}{2}}. \tag{2}$$

Estimating Equation 2 with the values used for Figure 4 gives $T_{\mathrm{N}} \approx 15$ months, which is relatively close, given the simplicity of the model, to the observed 12 month period. The small overshoot is probably due to the higher complexity of the full six-body problem. In addition, this analytic analysis predicts how would the oscillations change for different cyclone profiles and for different distances between cyclones (Figure S7 in Supporting Information S1), showing that the oscillations would only be observable for a narrow range of inter-cyclone distances.

2.3. Forced-Cyclones Model

To further illustrate how the described mechanism (Figure 3) results in the observed motion (Figure 2), a model that simulates the forces and the resulting trajectories of each cyclone with time is constructed. The model advances in time according to

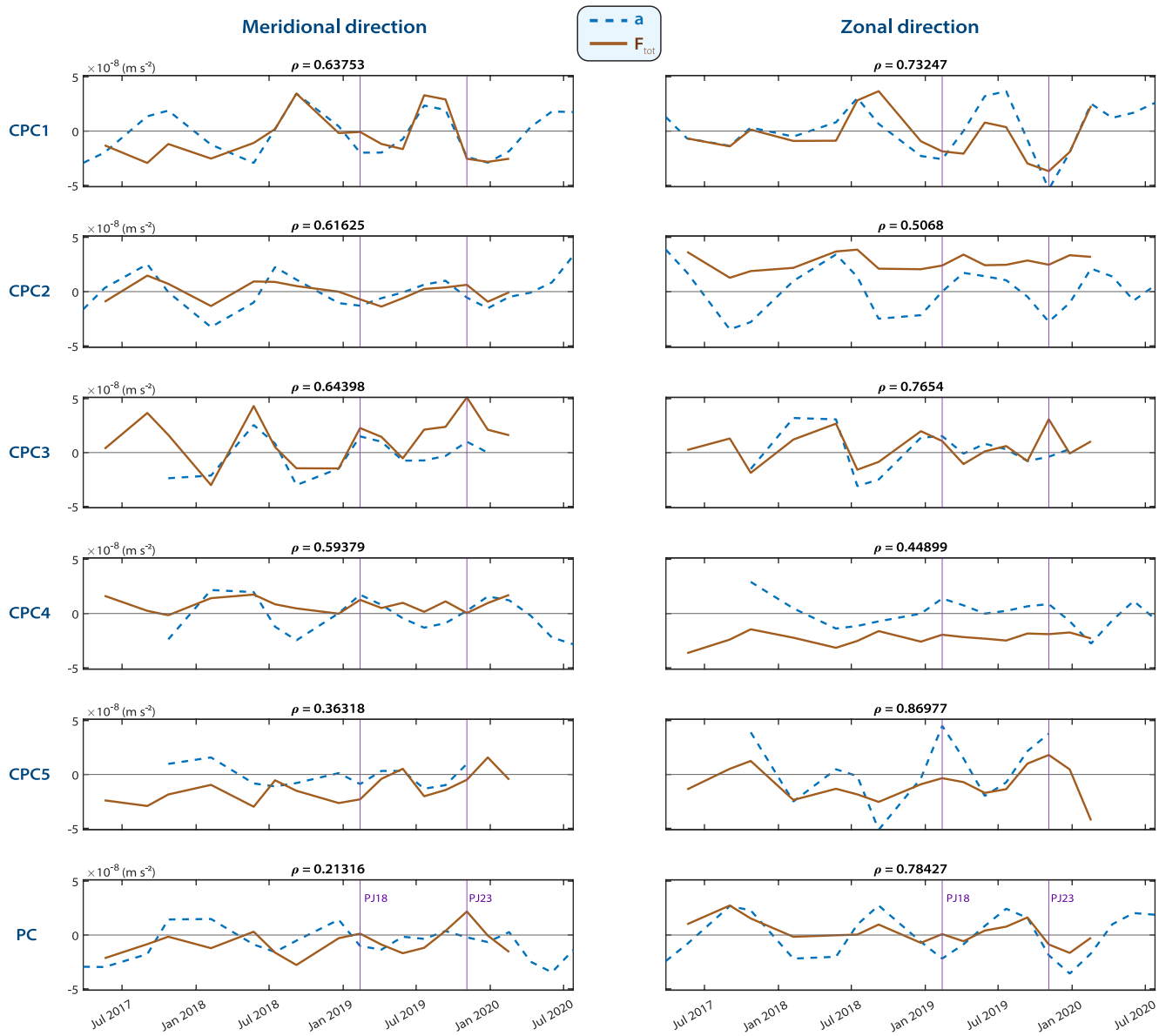

Figure 4. Comparison between the net force and the acceleration of the cyclones, using their instantaneous location data. Each panel represents a time series of the acceleration and force of one cyclone in one direction. Rows represent the different cyclones. The left column is in the meridional direction and the right column is in the zonal direction. The abscissa represents the observation's time. The ordinate, in units of (m s^{-2}), represents the amplitude of the two curves. The dashed blue curves are the acceleration of the cyclones, calculated by differentiating twice their observed positions with time. The brown lines represent the net force on the cyclones, resulting from the sum of the mutual cyclone rejection forces and F_β (Figure 3). The solid brown and dashed blue curves are expected to follow each other according to the suggested force balance. The Pearson correlation coefficient (ρ) between these two curves is presented above each panel.

$$\begin{aligned} \frac{\partial \mathbf{u}_i}{\partial t} &= \mathbf{a}_i, \\ \frac{\partial \mathbf{x}_i}{\partial t} &= \mathbf{u}_i, \end{aligned} \tag{3}$$

where t is time, $\boldsymbol{a}_i$, $\boldsymbol{u}_i$ and $\boldsymbol{x}_i$ are the acceleration (given by Equation 1), velocity and position vectors of cyclone i, respectively. For initial conditions, we use the observed locations of the cyclones at PJ4 (green crosses in Figure 2a), and for initial velocity we differentiate with time the locations during the first two observations. To find the unknown parameters, as described in the previous section, another optimization is performed, this time to get the simulated trajectories and spectra (Figure 5) as close as possible to the observations (Figure 2). The

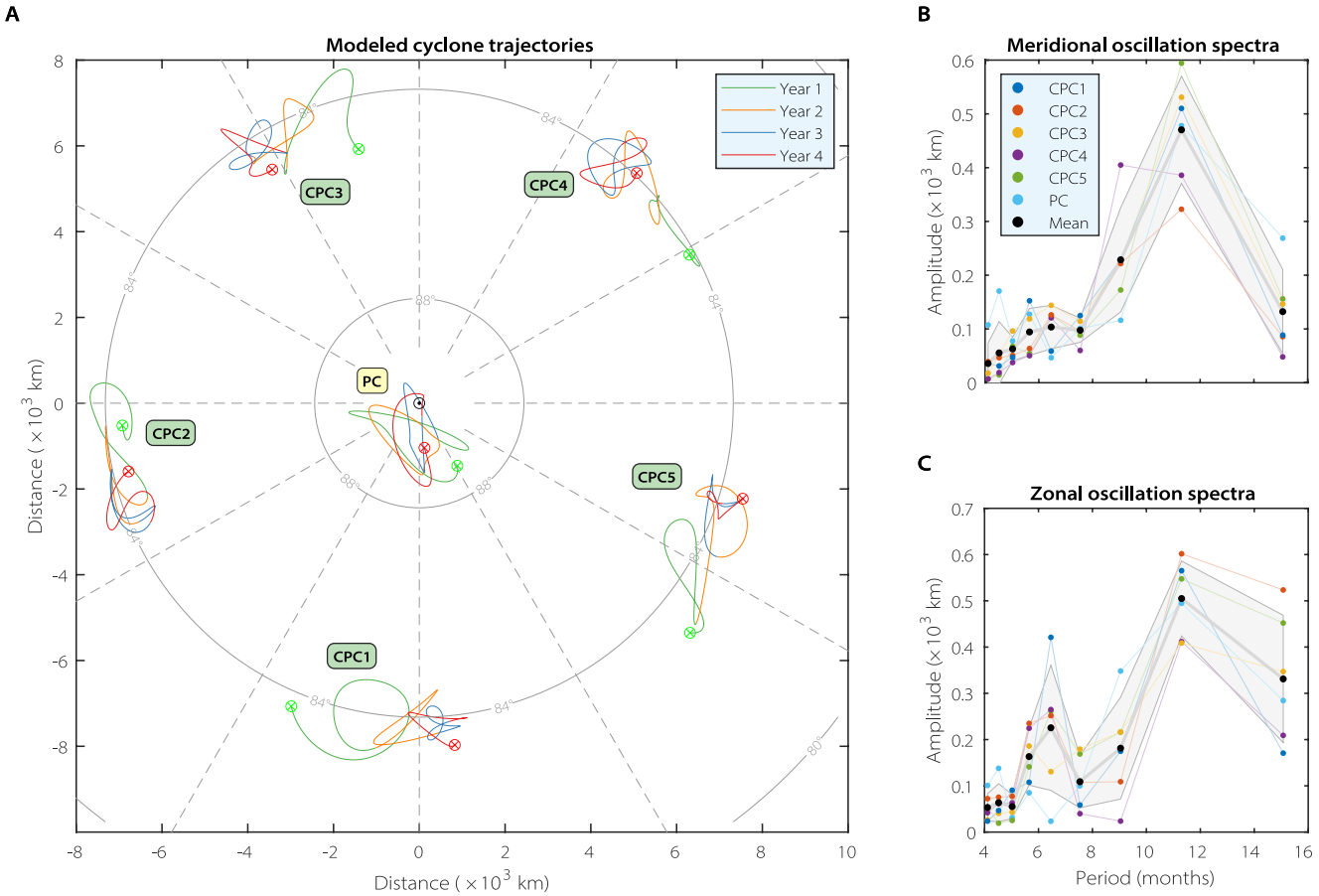

Figure 5. The modeled trajectories and spectra of Jupiter's south polar cyclones. (a) The trajectories of the modeled cyclones, moving in time according to Equations 1 and 3. The green 'X's denote the initial position of each cyclone, corresponding to the observed positions at PJ4. The red 'X's are the simulated final positions at PJ30. The trends change color after each year of simulation. See Movie S2 for an animation of the simulation results. (b and c) Zonal and meridional modeled oscillation spectra, respectively. The black dots and gray shades represent the mean and the 1 standard deviation range around it, respectively, calculated for each period between the six cyclones. These spectra are presented in terms of oscillation energy in Figure S8 of Supporting Information S1.

final values determined for these parameters and all other details of the model are described in Section S3 in Supporting Information S1.

As the model has no dissipation of energy, it is susceptible to resonances. However, dissipating the energy would mean that without also inserting energy, the motion would cease. To insert energy would require forcing the cyclones with artificial frequencies and amplitudes, thus biasing the model results. The optimization procedure, on the other hand, manages to avoid resonance by fine-tuning of the parameters, without insertion of additional terms to the forces balance. For this, the model cannot use the parameter values used for Figure 4, as it results in a resonant mode. Alternatively, using the model set for the analysis of Figure 4 shows good correlations, but the magnitudes have mismatches between the forces and the accelerations. Nevertheless, the differences between the final parameter sets of the two analyses (Figures 4 and 5) are relatively small, where both sets are within a reasonable physical range (see Table S1 in Supporting Information S1).

The model results (Figure 5) capture properly the observed motion patterns of the south polar cyclones (Figure 2). These patterns include both the form of their trajectories and the motion's spectra, which peak near 12 months with amplitudes of ~400 km. These model results exemplify that the mechanism described in this study (Figure 3) can, in fact, result in the observed motion. The similarity between the model and the observations adds additional support that the theory outlined in GK21 and here, can explain the transient motion of Jupiter's PCs and CPCs, in addition to describing their equilibrium states.

3. Discussion

By showing that vorticity gradients, induced both by the polar cyclones and by β, control the leading order balance of both the statistic steady-state (Gavriel & Kaspi, 2021) and the dynamic motion of the polar cyclones (Figure 4), we surmise that Jupiter's polar flow regime is largely barotropic, when looking at the scale of the cyclones (scales bigger than ∼500 km). This implies on the cyclones' depth, where either the thin SW equations, indicating on shallow cyclones, or deep 2D framework can capture the cyclone's motion. If the cyclones are indeed barotropic and deep, in agreement with the Taylor-Proudman theorem, they would extend uninterruptedly down to the semi-conducting region, where they would stop spinning due to magnetic drag (Dietrich & Jones, 2018; Duer et al., 2019; Kaspi et al., 2020; Liu et al., 2008). In this case, heat convection from Jupiter's core would be a plausible energy source for the cyclones (Cai et al., 2021; Garcia et al., 2020; Yadav & Bloxham, 2020; Yadav et al., 2020). These two options should come to mind when trying to analyze how the cyclones were formed, how they are maintained, and what determines their strength and morphology.

The north pole of Jupiter is expected to demonstrate similar dynamics for its cyclones as highlighted in this study for the south pole. However, as the available infrequent data do not allow a similar detailed analysis, this test is left for future studies, when more data might be gathered. For the south pole, while matching the cyclone's acceleration and position-based forces (Figure 4) required resolving unknown coefficients with an optimization procedure, the high correlations between them were found to be a robust feature, regardless of the determined values (within a sensible range, see Figure S5 in Supporting Information S1). For the robustness of the model simulation, unoptimized runs with simple assumptions and identical six cyclones also produce oscillation patterns similar to the observations (Figure S9 in Supporting Information S1). Overall, the results of both observational analysis (Figure 4) and of an idealized time-evolution model (Figure 5), establish the role of vorticity-gradient forces (Figure 3) as the driving mechanism of the Jovian south polar cyclones' observed motion (Figure 2), and highlight the importance of considering these forces in future studies on gas giants' polar dynamics and vortex motions at large.

Data Availability Statement

No new data sets were generated during the current study. The data analyzed in this study were published by Mura et al. (2021) (https://doi.org/10.1029/2021GL094235), as cited in the text. The figure files and Matlab scripts are available at: https://doi.org/10.5281/zenodo.6611745.

Acknowledgments
This research has been supported by the Minerva Foundation with funding from the Federal German Ministry for Education and Research and the Helen Kimmel Center for Planetary Science at the Weizmann Institute of Science.

References

Adriani, A., Bracco, A., Grassi, D., Moriconi, M., Mura, A., Orton, G., et al. (2020). Two-year observations of the Jupiter polar regions by JIRAM on board Juno. *Journal of Geophysical Research*, e2019JE006098.

Adriani, A., Mura, A., Orton, G., Hansen, C., Altieri, F., Moriconi, M., et al. (2018). Clusters of cyclones encircling Jupiter's poles. *Nature*, *555*(7695), 216–219. https://doi.org/10.1038/nature25491

Afanasyev, Y., & Huang, Y.-C. (2020). Poleward translation of vortices due to deep thermal convection on a rotating planet. *Geophysical & Astrophysical Fluid Dynamics*, *114*(6), 821–834. https://doi.org/10.1080/03091929.2019.1694676

Afanasyev, Y., & Zhang, Y. (2018). Cyclonic circulation of Saturn's atmosphere due to tilted convection. *Nature Geoscience*, *11*(3), 164–167. https://doi.org/10.1038/s41561-018-0070-3

Baines, K. H., Momary, T. W., Fletcher, L. N., Showman, A. P., Roos-Serote, M., Brown, R. H., et al. (2009). Saturn's north polar cyclone and hexagon at depth revealed by Cassini/VIMS. *Planetary and Space Science*, *57*(14–15), 1671–1681. https://doi.org/10.1016/j.pss.2009.06.026

Bolton, S. J., Adriani, A., Adumitroaie, V., Allison, M., Anderson, J., Atreya, S., et al. (2017). Jupiter's interior and deep atmosphere: The initial pole-to-pole passes with the Juno spacecraft. *Science*, *356*(6340), 821–825. https://doi.org/10.1126/science.aal2108

Brueshaber, S. R., & Sayanagi, K. M. (2021). Effects of forcing scale and intensity on the emergence and maintenance of polar vortices on Saturn and Ice Giants. *Icarus*, *361*, 114386. https://doi.org/10.1016/j.icarus.2021.114386

Brueshaber, S. R., Sayanagi, K. M., & Dowling, T. E. (2019). Dynamical regimes of giant planet polar vortices. *Icarus*, *323*, 46–61. https://doi.org/10.1016/j.icarus.2019.02.001

Cai, T., Chan, K. L., & Mayr, H. G. (2021). Deep, closely packed, long-lived cyclones on Jupiter's Poles. *The Planetary Science Journal*, *2*(2), 81. https://doi.org/10.3847/psj/abedbd

Chan, J., & Law, A. (1995). The interaction of binary vortices in a barotropic model. *Meteorology and Atmospheric Physics*, *56*(1), 135–155. https://doi.org/10.1007/bf01022526

Chan, J. C. (2005). The physics of tropical cyclone motion. *Annual Review of Fluid Mechanics*, *37*(1), 99–128. https://doi.org/10.1146/annurev.fluid.37.061903.175702

Dietrich, W., & Jones, C. A. (2018). Anelastic spherical dynamos with radially variable electrical conductivity. *Icarus*, *305*, 15–32. https://doi.org/10.1016/j.icarus.2018.01.003

Duer, K., Galanti, E., & Kaspi, Y. (2019). Analysis of Jupiter's deep jets combining Juno gravity and time-varying magnetic field measurements. *The Astrophysical Journal Letters*, *879*(2), L22. https://doi.org/10.3847/2041-8213/ab288e

Fine, K. S., Cass, A. C., Flynn, W. G., & Driscoll, C. F. (1995). Relaxation of 2D Turbulence to Vortex Crystals. *Physical Review Letters*, *75*(18), 3277–3280. https://doi.org/10.1103/physrevlett.75.3277

Fiorino, M., & Elsberry, R. L. (1989). Some aspects of vortex structure related to tropical cyclone motion. *Journal of the Atmospheric Sciences*, *46*(7), 975–990. https://doi.org/10.1175/1520-0469(1989)046<0975:saovsr>2.0.co;2

Franklin, J. L., Feuer, S. E., Kaplan, J., & Aberson, S. D. (1996). Tropical cyclone motion and surrounding flow relationships: Searching for beta gyres in omega dropwindsonde datasets. *Monthly Weather Review*, *124*(1), 64–84. https://doi.org/10.1175/1520-0493(1996)124<0064:tcmasf>2.0.co;2

Garcia, F., Chambers, F. R., & Watts, A. L. (2020). Deep model simulation of polar vortices in gas giant atmospheres. *Monthly Notices of the Royal Astronomical Society*, *499*(4), 4698–4715. https://doi.org/10.1093/mnras/staa2962

Gavriel, N., & Kaspi, Y. (2021). The number and location of Jupiter's circumpolar cyclones explained by vorticity dynamics. *Nature Geoscience*, *14*(8), 559–563. https://doi.org/10.1038/s41561-021-00781-6

Grassi, D., Adriani, A., Moriconi, M., Mura, A., Tabataba-Vakili, F., Ingersoll, A., et al. (2018). First estimate of wind fields in the Jupiter polar regions from JIRAM-Juno images. *Journal of Geophysical Research: Planets*, *123*, 1511–1524. https://doi.org/10.1029/2018je005555

Ingersoll, A., Ewald, S. P., Tosi, F., Adriani, A., Mura, A., Grassi, D., et al. (2021). *Polygonal patterns of cyclones on Jupiter: Convective forcing and anticyclonic shielding*. Research Square - Preprint.

Kaspi, Y., Galanti, E., Hubbard, W. B., Stevenson, D., Bolton, S., Iess, L., et al. (2018). Jupiter's atmospheric jet streams extend thousands of kilometres deep. *Nature*, *555*(7695), 223–226. https://doi.org/10.1038/nature25793

Kaspi, Y., Galanti, E., Showman, A. P., Stevenson, D. J., Guillot, T., Iess, L., & Bolton, S. J. (2020). Comparison of the deep atmospheric dynamics of Jupiter and Saturn in light of the Juno and Cassini gravity measurements. *Space Science Reviews*, *216*(5), 1–27. https://doi.org/10.1007/s11214-020-00705-7

LeBeau, R., & Dowling, T. (1998). EPIC simulations of time-dependent, three-dimensional vortices with application to Neptune's Great Dark Spot. *Icarus*, *132*(2), 239–265. https://doi.org/10.1006/icar.1998.5918

LeBeau, R., Farmer, K., Sankar, R., Hadland, N., & Palotai, C. (2020). A Numerical investigation of the Berg feature on Uranus as a vortex-driven system. *Atmosphere*, *11*(1), 52. https://doi.org/10.3390/atmos11010052

Li, C., Ingersoll, A. P., Klipfel, A. P., & Brettle, H. (2020). Modeling the stability of polygonal patterns of vortices at the poles of Jupiter as revealed by the Juno spacecraft. *Proceedings of the National Academy of Sciences of the United States of America*, *117*(39), 24082–24087. https://doi.org/10.1073/pnas.2008440117

Liu, J., Goldreich, P. M., & Stevenson, D. J. (2008). Constraints on deep-seated zonal winds inside Jupiter and Saturn. *Icarus*, *196*(2), 653–664. https://doi.org/10.1016/j.icarus.2007.11.036

Merlis, T. M., & Held, I. M. (2019). Aquaplanet simulations of tropical cyclones. *Current Climate Change Reports*, *5*(3), 185–195. https://doi.org/10.1007/s40641-019-00133-y

Moriconi, M., Migliorini, A., Altieri, F., Adriani, A., Mura, A., Orton, G., et al. (2020). Turbulence power spectra in regions surrounding Jupiter's south polar cyclones from Juno/JIRAM. *Journal of Geophysical Research: Planets*, *125*, e2019JE006096. https://doi.org/10.1029/2019je006096

Mura, A., Adriani, A., Bracco, A., Moriconi, M., Grassi, D., Plainaki, C., et al. (2021). Oscillations and stability of the Jupiter polar cyclones. *Geophysical Research Letters*, *48*(14), e2021GL094235. https://doi.org/10.1029/2021gl094235

O'Neill, M. E., Emanuel, K. A., & Flierl, G. R. (2015). Polar vortex formation in giant-planet atmospheres due to moist convection. *Nature Geoscience*, *8*(7), 523–526. https://doi.org/10.1038/ngeo2459

O'Neill, M. E., Emanuel, K. A., & Flierl, G. R. (2016). Weak jets and strong cyclones: Shallow-water modeling of giant planet polar caps. *Journal of the Atmospheric Sciences*, *73*(4), 1841–1855. https://doi.org/10.1175/jas-d-15-0314.1

Orton, G. S., Hansen, C., Caplinger, M., Ravine, M., Atreya, S., Ingersoll, A. P., et al. (2017). The first close-up images of Jupiter's polar regions: Results from the Juno mission JunoCam instrument. *Geophysical Research Letters*, *44*(10), 4599–4606. https://doi.org/10.1002/2016gl072443

Parisi, M., Kaspi, Y., Galanti, E., Durante, D., Bolton, S. J., Levin, S. M., et al. (2021). The depth of Jupiter's Great Red Spot constrained by Juno gravity overflights. *Science*, *374*(6570), 964–968. https://doi.org/10.1126/science.abf1396

Rivière, G., Arbogast, P., Lapeyre, G., & Maynard, K. (2012). A potential vorticity perspective on the motion of a mid-latitude winter storm. *Geophysical Research Letters*, *39*(12), 12808. https://doi.org/10.1029/2012gl052440

Rogers, J., Adamoli, G., Jacquesson, M., Vedovato, M., & Mettig, H. (2017). *Jupiter's high northern latitudes: Patterns and dynamics of the N3 to N6 domains*. JUPOS & BAA.

Rogers, J., Eichstädt, G., Hansen, C., Orton, G., Momary, T., Casely, A., et al. (2022). Flow patterns of Jupiter's south polar region. *Icarus*, *372*, 114742. https://doi.org/10.1016/j.icarus.2021.114742

Rossby, C. (1948). On displacements and intensity changes of atmospheric vortices. *Journal of Marine Research*, *7*(175), 71.

Sánchez-Lavega, A., Hueso, R., Hueso, R., Pérez-Hoyos, S., Rojas, J., & SAnchezlAvegA, A. (2006). A strong vortex in Saturn's south pole. *Icarus*, *184*(2), 524–531. https://doi.org/10.1016/j.icarus.2006.05.020

Schecter, D. A., Dubin, D. H. E., Fine, K. S., & Driscoll, C. F. (1999). Vortex crystals from 2D Euler flow: Experiment and simulation. *Physics of Fluids*, *11*(4),905–914. https://doi.org/10.1063/1.869961

Scott, R. (2011). Polar accumulation of cyclonic vorticity. *Geophysical & Astrophysical Fluid Dynamics*, *105*(4–5), 409–420. https://doi.org/10.1080/03091929.2010.509927

Shin, S.-E., Han, J.-Y., & Baik, J.-J. (2006). On the critical separation distance of binary vortices in a nondivergent barotropic atmosphere. *Journal of the Meteorological Society of Japan*, *84*(5), 853–869. https://doi.org/10.2151/jmsj.84.853

Siegelman, L., Klein, P., Ingersoll, A. P., Ewald, S. P., Young, W. R., Bracco, A., et al. (2022). Moist convection drives an upscale energy transfer at Jovian high latitudes. *Nature Physics*, *18*(3), 357–361. https://doi.org/10.1038/s41567-021-01458-y

Siegelman, L., Young, W. R., & Ingersoll, A. P. (2022). Polar vortex crystals: Emergence and structure. *Proceedings of the National Academy of Sciences*, *119*(17). https://doi.org/10.1073/pnas.2120486119

Sutyrin, G. G., & Flierl, G. R. (1994). Intense vortex motion on the beta plane: Development of the beta gyres. *Journal of the Atmospheric Sciences*, *51*(5), 773–790. https://doi.org/10.1175/1520-0469(1994)051<0773:ivmotb>2.0.co;2

Tabataba-Vakili, F., Rogers, J., Eichstadt, G., Orton, G., Hansen, C., Momary, T., et al. (2020). Long-term tracking of circumpolar cyclones on Jupiter from polar observations with JunoCam. *Icarus*, *335*, 113405. https://doi.org/10.1016/j.icarus.2019.113405

Vallis, G. K. (2017). *Atmospheric and oceanic fluid dynamics*. Cambridge University Press.

Yadav, R. K., & Bloxham, J. (2020). Deep rotating convection generates the polar hexagon on Saturn. *Proceedings of the National Academy of Sciences of the United States of America*, *117*(25), 13991–13996. https://doi.org/10.1073/pnas.2000317117

Yadav, R. K., Heimpel, M., & Bloxham, J. (2020). Deep convection–driven vortex formation on Jupiter and Saturn. *Science Advances*, *6*(46), eabb9298. https://doi.org/10.1126/sciadv.abb9298

Zhao, H., Wu, L., & Zhou, W. (2009). Observational relationship of climatologic beta drift with large-scale environmental flows. *Geophysical Research Letters*, *36*(18), L18809. https://doi.org/10.1029/2009gl040126

References From the Supporting Information

Chan, J. C., & Williams, R. (1987). Analytical and numerical studies of the beta-effect in tropical cyclone motion. Part I: Zero mean flow. *Journal of the Atmospheric Sciences*, *44*(9), 1257–1265. https://doi.org/10.1175/1520-0469(1987)044<1257:aansot>2.0.co;2